Supplemental Information for

Minimal cobalt metabolism in the marine cyanobacterium Prochlorococcus

Nicholas J. Hawco[1,2,†,*], Matthew M. McIlvin[1], Randelle M. Bundy[1,3], Alessandro Tagliabue[4], Tyler J. Goepfert[1,5], Dawn M. Moran[1], Luis Valentin-Alvarado[1,6], Giacomo R. DiTullio[7] and Mak A. Saito[1*]

[1] Department of Marine Chemistry and Geochemistry, Woods Hole Oceanographic Institution, Woods Hole MA, USA
[2] Department of Earth Sciences, University of Southern California, Los Angeles CA, USA
[3] School of Oceanography, University of Washington, Seattle WA, USA
[4] Department of Earth, Ocean and Ecological Sciences, University of Liverpool, Liverpool UK
[5] School of Earth and Space Exploration, Arizona State University, Tempe AZ, USA
[6] Department of Plant and Microbial Biology, University of California at Berkeley, Berkeley CA USA
[7] Hollings Marine Lab, College of Charleston, Charleston SC, USA

[†]Present address: Department of Oceanography, University of Hawaii at Manoa, Honolulu HI

* Corresponding Authors. Contact: hawco@hawaii.edu, 1000 Pope Road, 808-956-2613; msaito@whoi.edu, 266 Woods Hole Road MS#51, 508-289-2393.

This PDF file includes:

1. Supplemental Methods
2. Supplemental References
3. Supplemental Figures S1- S11
4. Supplemental Tables S1 to S8

1. Supplemental methods

Culturing procedures

Prochlorococcus strain MIT9215 was originally isolated from the Equatorial Pacific in Oct. 1992 (1). Axenic cultures were provided by the Chisholm lab at MIT and grown at 27°C in a custom incubator under a 14:10 light:dark cycle at a peak light intensity of 75 μmol photon m^{-2} s^{-1}. For all experiments, cells were inoculated at 1% media volume or lower from cultures in mid-late exponential phase. Growth was monitored by *in vivo* chlorophyll fluorescence. Cultures were grown in a modified ProTM media (2) where concentrations of inorganic metal species (denoted as metal') are stabilized by equilibrium with ethylenediamine tetraacetic acid (EDTA) (3). At an EDTA concentration of 11.7 μM, the ratio of Fe' to total iron is $10^{-1.94}$ and the ratio of Co' to total cobalt is $10^{-2.81}$ (4). Background iron and cobalt concentrations were determined to be 0.3 and 0.01 nM, respectively. For all experiments, Fe' (maximum 135 pM) was below Fe hydroxide solubility thresholds (~500 pM (5)).

Cells were harvested by centrifugation, digested in 5% nitric acid, and analyzed by ICP-MS (4). Samples were corrected for matrix effects using a 1ppb In internal standard and calibrated relative to a 1-100 ppb standard curve made from a certified multielement standard (Spex Certiprep). Duplicate analyses of cell digests agreed within 5% for both Co and Fe, except at Co levels below 30 atoms per cell which agreed to ~20%. Process blanks were subtracted from measured concentrations. The mean blank for this dataset was 0.022 pmol for Co and 12.4 pmol for Fe. Detection limits (as 3-times the standard deviation of the blank, n=12) were 0.044 pmol for Co and 30 pmol for Fe. Phosphorus concentrations were also measured by ICP-MS and calibrated to a separate standard curve ranging from 100–1500 ppb sodium phosphate, which was cross-calibrated to a certified 1 ppm P standard (Alfa Aesar Specpure). Metal and P concentrations in digestions were scaled to original culture volume and divided by cell number to derive per cell quotas. Harvested cells were not washed with chelating solutions (6) to remove extracellularly-bound metals, but low Fe' concentrations used in these experiments suggest minimal Fe precipitation onto cell surfaces, consistent with laboratory validation studies (7).

For all samples where quotas were measured, cell number was determined by flow cytometry on a Guava Easycyte HT instrument with Incyte 3.1 software. Cultures were serially diluted in filtered oligotrophic seawater and counted using a red fluorescence gate until 5000 events were recorded. This instrument was calibrated monthly with beads. Dilutions with cell concentrations in the range of 0.5–2 x 10^5 cells per ml were used to calculate original cell number. No difference was observed in cell number of nutrient replete, exponential phase cultures preserved with 5% paraformaldehyde, flash frozen in liquid nitrogen and stored at -80 °C (cobalt-limitation series, 5.3 x 10^7 cells/ml) versus cells that were frozen directly at -80 °C (iron-limitation series, 5.5 x 10^7 cells/ml). Cell density of media supernatant following centrifugation was also measured to evaluate harvesting efficiency by this method. In general, harvesting efficiency by centrifugation was >95%, except at low cell densities where harvesting efficiency was still >80%. Agreement between cellular P quotas (1.1 ± 0.4 x 10^7 atoms per cell, Table S2) and literature data for this strain (0.4-0.7 x 10^7 atoms per cell (8)) and *Prochlorococcus* Med4 (0.2–2 x 10^7 atoms per cell (9)), indicate that ICPMS and flow cytometry determinations are robust. The 1.7 M bp genome of *Prochlorococcus* MIT9215 alone accounts for 0.3 x 10^7 P atoms per cell, a considerable fraction of the cellular P quota. Metal:C ratios were

estimated as the mean of two approaches: 1) a conversion of metal cell^{-1} quotas using a C cell^{-1} quota ($1.85 \pm 0.23 \times 10^9$ C atoms cell^{-1}) and 2) the product of the metal:P ratio and the P:C ratio (325 ± 74 mol:mol). Both conversion factors reflect published measurements of the *Prochlorococcus* MIT9215 strain (8) and uncertainties are propagated throughout.

Additional culturing protocols, plasticware cleaning procedures, media preparation, and measurement of growth rates and cell quotas are identical to those described by Hawco and Saito (2018) and methodological details can be found there (4). All curve fitting was performed with using least-squares routines in Sigma Plot 12.

Protein Extraction and Global Proteomic Analysis

Soluble proteins were extracted from cell pellets and digested using a detergent-free method (10). Biomass was resuspended in 100 mM ammonium bicarbonate and sonicated on ice at 70% duty for two 4-minute intervals and then centrifuged at 14,000 rpm for 20 minutes at 4°C. 200 µl of supernatant was precipitated in 800 µl acetone at -20°C for several days. The supernatant solution was removed after spinning at 14,000 rpm at 4°C and precipitated proteins were dried on a speed-vac (Thermo) for several minutes.

Extracted protein was resuspended with 125 µl of 6M urea in 100 mM ammonium bicarbonate and heated to 95°C to dissolve. 100 µl of this sample was then incubated with 5 µl of 200 mM dithiothreitol (DTT) for 1 hour at 56°C, 20 µl of 200 mM iodoacetamide for 1 hour at room temperature, and finally for 1 hour at room temperature with an additional 20 µl of 200 mM DTT. Samples were diluted to 1 ml in 100 mM ammonium bicarbonate and trypsin (Promega Gold) was added at a 1:50 ratio to total protein, quantified by a detergent compatible (DC) colorimetric assay (Bio-Rad) at 750 nm on a UV-Vis spectrophotometer (Shimadzu). Samples were digested overnight at 37°C. Peptides were concentrated by speed-vac and then diluted with an LC-MS buffer containing 98% water, 2% acetonitrile, and 0.1% formic acid to a final protein concentration of 0.1 µg/µl.

Global proteome composition was analyzed by liquid chromatography mass spectrometry (LC-MS) following previously described procedures (11). Protein extracts were analyzed in duplicate. Raw mass spectrometry files were searched using *Prochlorococcus* MIT9215 genome (downloaded from NCBI) and scored through the Sequest algorithm using Proteome Discoverer software (Thermo). Mass tolerance settings of 10 ppm for parent ions and 0.02 Da for fragments were used with fixed cysteine carbamidomethylation (+57), variable methionine oxidation (+16), and a maximum of 2 missed trypsin cleavages. Processed data were assembled and spectra were counted using Scaffold 4.7.3 with 95% minimum peptide thresholds and 99.9% minimum protein thresholds applied. False discovery rates for the cobalt gradient experiment (10, 3, 1 and 0.6 nM Co) was calculated to be 0.2% for decoy peptides and 5.5% for decoy proteins.

A Fisher's Exact test was applied to 584 detected proteins to compare spectral counts between cobalt-limited samples (0.6 and 1 nM Co) and cobalt replete samples (3 and 10 nM Co) with significance being determined at $p<0.01$. Prior to plotting, this dataset was reduced by eliminating proteins that were not identified in each of the 4 samples (2 treatments with 2 technical replicates) within the cobalt-limited or cobalt-replete groups. Figure S2B shows the 121 proteins that meet these criteria, 20 of which were significantly more abundant and 14 of which were significant less abundant (Table S9), with error bars in Fig. S2B reflecting the standard deviation between 4 samples.

Quantitative Protein Measurements of NrdJ and MetH

Due to their low abundance, neither NrdJ nor MetH were detected using the strict settings needed to interpret global proteomes. Instead, *Prochlorococcus* MIT9215 methionine synthase (*metH*, P9215_10151) and ribonucleotide reductase (*nrdJ*, 9215_07641) peptides were quantified by selected reaction monitoring (SRM) by targeted liquid chromatography mass spectrometry, which required additional *Prochlorococcus* biomass and the generation of isotopically labeled standards.

Large volume cultures of cobalt-limited *Prochlorococcus* MIT9215 cultures (non-axenic) were grown in 8 L polycarbonate carboys and sampled over several days during exponential growth. Four 30 mL aliquots were taken at the start of exponential phase and grown in 28 mL polycarbonate tubes alongside larger carboys to measure growth rate under similar light and media conditions. Growth rates increased when additional cobalt was added to two of these aliquots to validate that cells were indeed limited by cobalt.

Chlorophyll fluorescence of aliquots collected in 8 L carboys during sample harvesting agreed with levels in 28 mL cultures, suggesting that growth in both bottles grew similarly over these short timescales (<7 days). Biomass for metal and protein measurements was harvested simultaneously. In addition to measuring cellular cobalt quotas in these samples (described above), the cobalt content of the acetone supernatant during protein extraction was measured after evaporating to dryness by speed-vac and digesting in 5% nitric acid. The cobalt concentration in these aliquots indicated that between 30– 70% of the cobalt quota was released during sonication and, by inference, a similar percentage of cobalt-bearing proteins. It is likely that a greater fraction of NrdJ and MetH were extracted. Biochemical studies with homologous enzymes have demonstrated that both proteins are soluble in aqueous solution, suggesting that the protein extraction procedure employed is able to recover these enzymes (12, 13). Because detergent-free protein extractions discriminate against lipophilic proteins associated with plasma or photosynthetic membranes, cobalt bound to these proteins may account for the 'missing' cobalt quota. This may include cobalt-bearing intermediates of the B_{12} biosynthetic pathway, which is probably membrane bound (14). However, the higher reagent blanks associated with measuring cobalt in protein extracts compared to acid digestions make the former determinations more uncertain.

Isotope labeled peptide standards were generated by overexpression of a pET30-a plasmid with sequences for *Prochlorococcus nrdJ*, *metH* and horse myoglobin peptides (Fig. S9) in competent *E. coli* cells (Novagen Tuner(DE3) pLysS). Individual colonies were selected and grown in 10 mL of ^{15}N-labeled media (Cambridge Isotope Laboratories Bioexpress Cell Growth Media U-15N, 98%) amended with 100 mg L^{-1} kanamycin, overnight at 34°C. Afterwards, 100 µL of cells were inoculated into 10 mL of ^{15}N labeled media and induced with 1 mM IPTG after 3 hours at 34°C. Induced cells were harvested after 24 hours at 20°C by centrifugation at 6500 g for 20 min at 4°C and frozen at -20°C. Cell pellets were then lysed with 1 mL soluble lysis reagent (Novagen Bug Buster protein extraction reagent amended with 25 units of Benzonase Nuclease) and centrifuged at 6500 g for 20 min at 4°C, after which the supernatant solution was decanted from the pellet of inclusion bodies. Inclusion bodies were dissolved in 6M urea and digested with trypsin according to the above protocol. Labeled peptides were analyzed by LC-MS to ensure complete trypsin digestion and the absence of detectible peptides with natural isotope abundance. A manuscript describing this method in detail is forthcoming (McIlvin and Saito, *in prep*.)

Labeled peptides were calibrated relative to commercial horse myoglobin (Fischer), which was resuspended in ammonium bicarbonate to 100 nM and digested overnight with 6 µg trypsin at room temperature. Addition of a known quantity of commercial horse myoglobin peptides (unlabeled) was used to quantify the concentration of ^{15}N-labeled myoglobin peptides that were overexpressed in *E. coli* (Table S6). Because ^{15}N-labeled *Prochlorococcus* peptides and ^{15}N- labeled myoglobin peptides were cloned from a single sequence, the measured concentration of ^{15}N-labeled myoglobin peptides is equal to the concentration of ^{15}N-labeled *Prochlorococcus* NrdJ and MetH peptides. Digested, ^{15}N-labeled peptides were added to digested *Prochlorococcus* peptides (0.1 µg/µl total protein) to a final concentration of 3.3 fmol/µl of labeled peptide. 10 µl of sample was injected onto a 5 µm C18 peptide trap connected to a 3 µm C18 column. Peptides were separated with a Microhm Advance liquid chromatography system over a gradient of 0-95% acetonitrile over a 40 minute window. This gradient increased linearly from 2 to 40% over the first 30 minutes and increased to 95% acetonitrile over the next 5 minutes. Secondary mass spectra (MS^2) were collected with a Q-Exactive mass spectrometer (Thermo) using an inclusion list containing both heavy and light peptide masses. The ratio of labeled and unlabeled peptides was then used to determine the concentration of NrdJ and MetH in protein digests (fmol/µg protein digested, Table S7, Figs. S10, S11). Skyline targeted proteomics software (https://skyline.ms/project/home/begin.view?) was used to process MS^2 spectra and calculate peptide ratios.

Peptide concentrations were corrected for dilution and sample splitting during protein digestion to arrive at a cellular quota. We excluded two of the six peptides that were cloned for each enzyme due to anomalously low sensitivity of labeled standards or poor peak resolution in samples. The concentration of remaining peptides agreed to a reasonable extent (~20%) with relative abundance trends between samples being more consistent.

Following measurement of these proteins in large volume *Prochlorococcus* MIT9215 cultures, NrdJ and MetH abundance was determined in protein extracts from the cobalt-gradient experiment (10, 3, 1, 0.6 nM Co). The relative abundance of NrdJ and MetH in these samples was quantified (e.g. Fig. S2A) but could not be reliably related to a cellular quota due to low extraction/retention efficiency at low protein concentration in these samples. The ratio of NrdJ to MetH peptides was similar between large volume cobalt-limited cultures (2.3) and cobalt-limited cultures from the Co gradient experiment (2.9), suggesting that relative abundance measurements for this dataset are robust (Table S7)

Dissolved and particulate cobalt distributions in the Equatorial Pacific Ocean.

The Metzyme cruise (KM1128) was conducted during October 2011, between Honolulu, Hawai`i and Apia, Western Samoa. The transect followed a North-South line at 155 °W to the equator and proceeded to the southwest to 15°S, 170°W (Fig. 2A). Trace metal clean sampling procedures and nutrient analyses have been fully described by Saito et al., 2014 (15). Samples for dissolved cobalt determinations were 0.2 µm filtered with 47 mm Supor filters (saved for particulate analyses) in a clean space maintained by HEPA air filtration. Filtered samples were stored in 60 ml acid-clean polyethylene bottles at 4 °C and preserved with metal-free gas absorbing satchels (Mitsubishi Gas and Chemical) in heat sealed bags, with 3 satchels and 6 samples per bag.

Dissolved cobalt concentrations were determined by cathodic stripping voltammetry (CSV) using dimethylglyoxime (DMG) as a competing ligand following UV-oxidation to destroy organic cobalt ligands (16). Cobalt profiles from stations 1 (17°N), 3 (8°N), and 5 (0°N)

were published previously (15). All other samples were measured concurrently with dissolved cobalt for samples for that GEOTRACES GP16 dataset, following identical analytical procedures (17). During this time, stations 1, 3, and 5 were re-run and agreed with published values for these samples, except for samples from the oxygen minimum zone in Station 3 (8°N), where some cobalt (~20 pM) seemed to have been lost over ~2 years since removal from O_2-free bags, an effect that has been documented in the oxygen minimum zone of the North Atlantic (18). A blank of 4.6 pM ± 0.7 pM Co was determined from 19 analyses of Chelex-100 treated, UV oxidized seawater (16). This blank reflects cobalt added from reagents and other sources during analyses. The detection limit of this dataset, calculated as 3-times the standard deviation of the blank, was 2.1 pM. Ocean sections in Figure 2 made using Ocean Data View version 4.7.10 (Schlitzer, R., https://odv.awi.de).

Particulate cobalt and particulate phosphate were measured on 0.2 μm Supor filters (47 mm) used for filtering seawater collected in 8 L X-Niskin bottles (15). Filters returned to the lab frozen and were digested in 50% trace metal grade nitric acid with 1ppb Indium at 90 °C for 3 hours, diluted to 5% nitric acid with ultrapure water (Milli-Q), and analyzed on an Element 2 mass spectrometer in the WHOI ICP-MS facility. Indium was used as an internal standard to correct for sample injection and dilution. The instrument was calibrated using external standards diluted from certified standards (SPEX Certiprep) and filter blanks were subtracted from measured values.

Analyses with the PISCES Cobalt Biogeochemical Model

Field observations of seawater Co:P stoichiometry were extrapolated to the global ocean using a recently developed biogeochemical model of the marine cobalt cycle (19). This model operates within the PISCES biogeochemical framework (20). All cobalt-related parametrizations are added without feedback to the base model (i.e. no feedbacks on phytoplankton growth, macronutrient uptake etc.). The cobalt model was rerun following an update to the underlying biogeochemical descriptions of the PISCES model to incorporate new descriptions of POC flux and remineralization (21). Despite no new changes to Co-related parametrizations, the new simulations represent an improved fit to observations compared to the published model and produce lower cobalt concentrations in the surface of the South Pacific Ocean, consistent with measured values.

To determine the total metal:phosphorus ratio for surface ocean grid cells, cobalt, iron and P pools across dissolved and particulate phases were summed. Grid cells with mean annual temperatures below 12°C were excluded from analysis because culture and field evidence suggest *Prochlorococcus* is not found in these waters (22). Model data are plotted in Figs. 4, S5, S6, and S8.

The fidelity of modelled Co:P and Fe:P ratios was assessed by comparison to high-quality cobalt, iron and phosphate measurements compiled in the GEOTRACES Intermediate Data Product 2017 (23). Co-located Fe, Co, and P concentrations from the upper 30 m of the ocean were extracted (n = 231). This depth range was chosen to maximize the number of samples while avoiding upwelling signals derived from the nutricline. Of these measurements, 33 had Co:PO4 ratios below 26 μmol:mol, mostly from the GP16 transect in the Eastern Tropical South Pacific (17). Because of significant uncertainty in these parameters at very low concentrations, minimum concentrations of 3 pM Co, 50 pM Fe, and 20 nM P were imposed. Note that because this database only includes PO_4 measurements, this threshold helps to acknowledge the presence of bioavailable dissolved organic phosphorus that supports

phytoplankton growth at extremely low PO_4. The choice of these lower limits does not have a meaningful impact on the distribution of data in Figure 4.

4. Supplemental references

1. Moore LR, Chisholm SW (1999) Photophysiology of the marine cyanobacterium *Prochlorococcus*: ecotypic differences among cultured isolates. *Limnol Oceanogr* 44(3):628–638.
2. Moore LR, et al. (2007) Culturing the marine cyanobacterium *Prochlorococcus*. *Limnol Oceanogr Methods* 5:353–362.
3. Sunda W, Price N, Morel F (2005) Trace metal ion buffers and their use in culture studies. *Algal Culturing Techniques* (Academic Press), pp 35–63.
4. Hawco NJ, Saito MA (2018) Competitive inhibition of cobalt uptake by zinc and manganese in a pacific *Prochlorococcus* strain : Insights into metal homeostasis in a streamlined oligotrophic cyanobacterium. *Limnol Oceanogr* 63:2229–2249.
5. Sunda WG, Huntsman SA (1997) Interrelated influence of iron, light and cell size on marine phytoplankton growth. *Nature* 390(6658):389–392.
6. Tang D, Morel FMM (2006) Distinguishing between cellular and Fe-oxide-associated trace elements in phytoplankton. *Mar Chem* 98(1):18–30.
7. Ho T, et al. (2003) The elemental composition of some marine phytoplankton. *J Phycol* 39(6):1145–1159.
8. Martiny AC, Ma L, Mouginot C, Chandler JW, Zinser ER (2016) Interactions between thermal acclimation, growth rate, and phylogeny influence *Prochlorococcus* elemental stoichiometry. *PLoS One* 11(12):e0168291.
9. Bertilsson S, Berglund O, Karl DM, Chisholm SW (2003) Elemental composition of marine *Prochlorococcus* and *Synechococcus*: Implications for the ecological stoichiometry of the sea. *Limnol Oceanogr* 48(5):1721–1731.
10. Cox AD, Saito MA (2013) Proteomic responses of oceanic Synechococcus WH8102 to phosphate and zinc scarcity and cadmium additions. *Front Microbiol* 4(DEC):1–17.
11. Mackey KRM, et al. (2015) Divergent responses of Atlantic coastal and oceanic *Synechococcus* to iron limitation. *Proc Natl Acad Sci* 112(32):9944–9949.
12. Goulding CW, Matthews RG (1997) Cobalamin-dependent methionine synthase from Escherichia coli: Involvement of zinc in homocysteine activation. *Biochemistry* 36(50):15749–15757.
13. Licht SS, Lawrence CC, Stubbe J (1999) Class II ribonucleotide reductases catalyze carbon-cobalt bond reformation on every turnover. *J Am Chem Soc* 121(33):7463–7468.
14. Patterson CJ, et al. (2013) Co(ii)-detection does not follow Kco(ii) gradient: channelling in Co(ii)-sensing. *Metallomics* 5(4):352–362.
15. Saito MA, et al. (2014) Multiple nutrient stresses at intersecting Pacific Ocean biomes detected by protein biomarkers. *Science (80)* 345(6201):1173–1177.
16. Saito MA, Moffett JW (2001) Complexation of cobalt by natural organic ligands in the Sargasso Sea as determined by a new high-sensitivity electrochemical cobalt speciation method suitable for open ocean work. *Mar Chem* 75(1–2):49–68.
17. Hawco NJ, Ohnemus DC, Resing JA, Twining BS, Saito MA (2016) A cobalt plume in the oxygen minimum zone of the Eastern Tropical South Pacific. *Biogeosciences*

13:5697–5717.
18. Noble AE, Ohnemus DC, Hawco NJ, Lam PJ, Saito MA (2017) Coastal sources, sinks and strong organic complexation of dissolved cobalt within the US North Atlantic GEOTRACES transect GA03. *Biogeosciences* 14(11):2715–2739.
19. Tagliabue A, et al. (2018) The Role of External Inputs and Internal Cycling in Shaping the Global Ocean Cobalt Distribution: Insights From the First Cobalt Biogeochemical Model. *Global Biogeochem Cycles* 32(4):594–616.
20. Aumont O, Ethe C, Tagliabue A, Bopp L, Gehlen M (2015) PISCES-v2 : an ocean biogeochemical model for carbon and ecosystme studies. *Geosci Model Dev* 8:2465–2513.
21. Aumont O, et al. (2017) Variable reactivity of particulate organic matter in a global ocean biogeochemical model. *Biogeosciences* 14(9):2321–2341.
22. Zinser ER, et al. (2007) Influence of light and temperature on *Prochlorococcus* ecotype distributions in the Atlantic Ocean. *Limnol Oceanogr* 52(5):2205–2220.
23. Schlitzer R, et al. (2018) The GEOTRACES Intermediate Data Product 2017. *Chem Geol* 493:210–223.
24. Rii YM, Karl DM, Church MJ (2016) Temporal and vertical variability in picophytoplankton primary productivity in the North Pacific Subtropical Gyre. *Mar Ecol Prog Ser* 562:1–18.
25. Malmstrom RR, et al. (2010) Temporal dynamics of *Prochlorococcus* ecotypes in the Atlantic and Pacific oceans. *ISME J* 4(10):1252.
26. Xu Y, Tang D, Shaked Y, Morel FMM (2007) Zinc, cadmium, and cobalt interreplacement and relative use efficiencies in the coccolithophore *Emiliania huxleyi.* *Limnol Oceanogr* 52(5):2294–2305.
27. Webb EA, Moffett JW, Waterbury JB (2001) Iron stress in open-ocean cyanobacteria (*Synechococcus, Trichodesmium,* and *Crocosphaera spp*.): Identification of the idia protein. *Appl Environ Microbiol* 67(12):5444–5452.
28. Raven JA (1990) Predictions of Mn and Fe use efficiencies of phototrophic growth as a function of light availability for growth and of C assimilation pathway. *New Phytol* 116(1):1–18.
29. Raven JA (1988) The iron and molybdenum use efficiencies of plant growth with different energy, carbon and nitrogen sources. *New Phytol* 109(3):279–288.
30. Sintchak MD, Arjara G, Kellogg BA, Stubbe J, Drennan CL (2002) The crystal structure of class II ribonucleotide reductase reveals how an allosterically regulated monomer mimics a dimer. *Nat Struct Mol Biol* 9(4):293.
31. Kettler GC, et al. (2007) Patterns and implications of gene gain and loss in the evolution of *Prochlorococcus*. *PLoS Genet* 3(12):e231.
32. Drennan CL, Huang S, Drummond JT, Matthews RG, Ludwig ML (1994) How a protein binds B_{12}: a 3.0 Å X-ray structure of B_{12}-binding domains of methionine synthase. *Science* 266(5191):1669–74.
33. Banerjee R V, Frasca V, Ballou DP, Matthews RG (1990) Participation of cob(I) alamin in the reaction catalyzed by methionine synthase from *Escherichia coli*: a steady-state and rapid reaction kinetic analysis. *Biochemistry* 29(50):11101–9.
34. Heldal M, Scanlan DJ, Norland S, Thingstad F, Mann NH (2003) Elemental composition of single cells of various strains of marine *Prochlorococcus* and *Synechococcus* using X-ray microanalysis. *Limnol Oceanogr* 48(5):1732–1743.

3. Supplemental figures

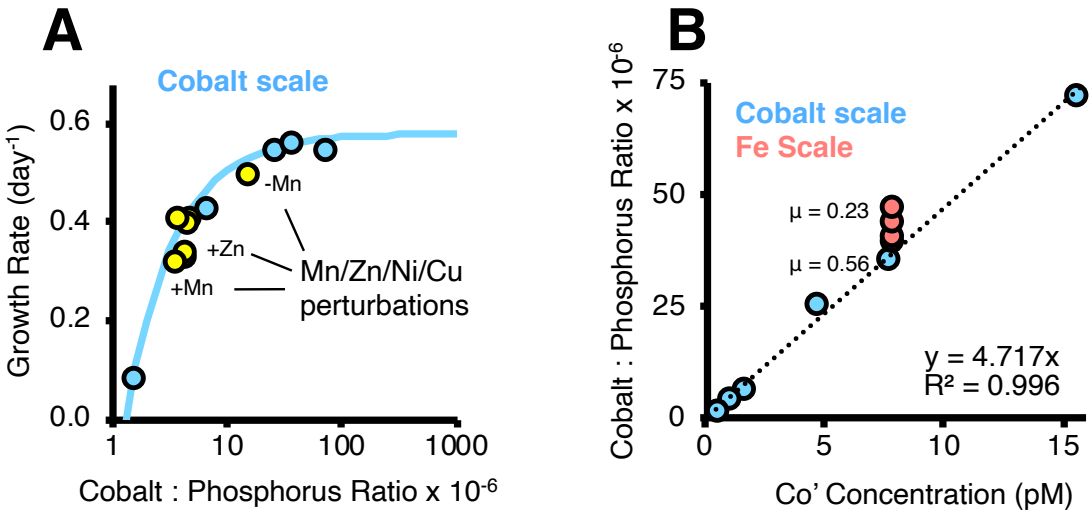

Figure S1. A) Growth of *Prochlorococcus* MIT9215 cultures as a function of the cellular Co:P ratio. Blue points show results from experiments where Co' concentration was varied but all other metals were held constant. The blue line shows a fit of the Droop Curve for these data (R^2 = 0.96, see Table S1). Yellow circles show results from metal perturbation experiments under a constant, limiting concentration of Co' (4). Media with additional Mn and Zn depressed growth rates while media with less added Mn increased growth rates. Additional treatments (+Ni, -Ni, +Cu) did not strongly affect growth and are unlabeled. Note the similarity between Co:P ratio and growth rate in both sets of experiments implies that Zn/Mn effects are primarily associated with competitive inhibition at the transporter site and not intracellular toxicity (see Hawco and Saito 2018). B) Evidence for additional Co uptake by *Prochlorococcus* under Fe limitation. Blue circles show linear relationship between cellular Co:P and the media Co' concentration (R^2 >0.99). Red circles show Co:P ratio as cells become more Fe limited. Note that Co' in these experiments is held constant.

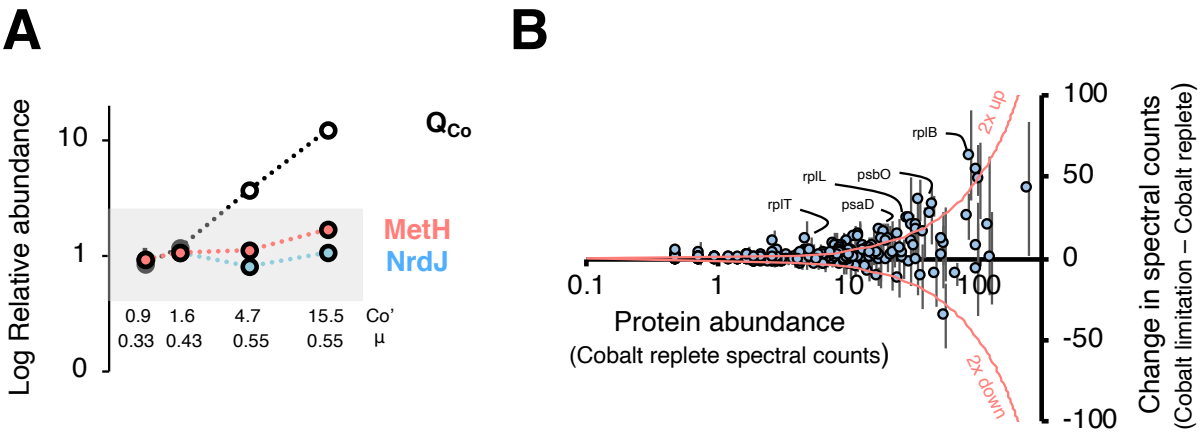

Figure S2. Proteomic measurements of cobalt-limited metabolism of *Prochlorococcus* MIT9215. A) Relative abundance of cobalamin-dependent ribonucleotide reductase (NrdJ, blue circles) and cobalamin-dependent methionine synthase (MetH, red circles) as a function of growth rate and cobalt concentration, determined by selected reaction monitoring of four tryptic peptides. White circles show relative change in the cellular cobalt quota, Q_{Co}, which has a maximum value of 780 atoms per cell. B) Whole cell proteomes under cobalt limitation. Vertical axis reflects the difference in assigned spectral counts in cobalt-limited samples (0.3 and 1.6 pM Co') relative to cobalt-replete samples (4.7 and 15.5 pM Co'), with positive values reflecting upregulation under cobalt limitation. Red lines follow trajectories of a two-fold up- or down-regulation. Select up-regulated proteins are annotated (see Table S8 for a complete list).

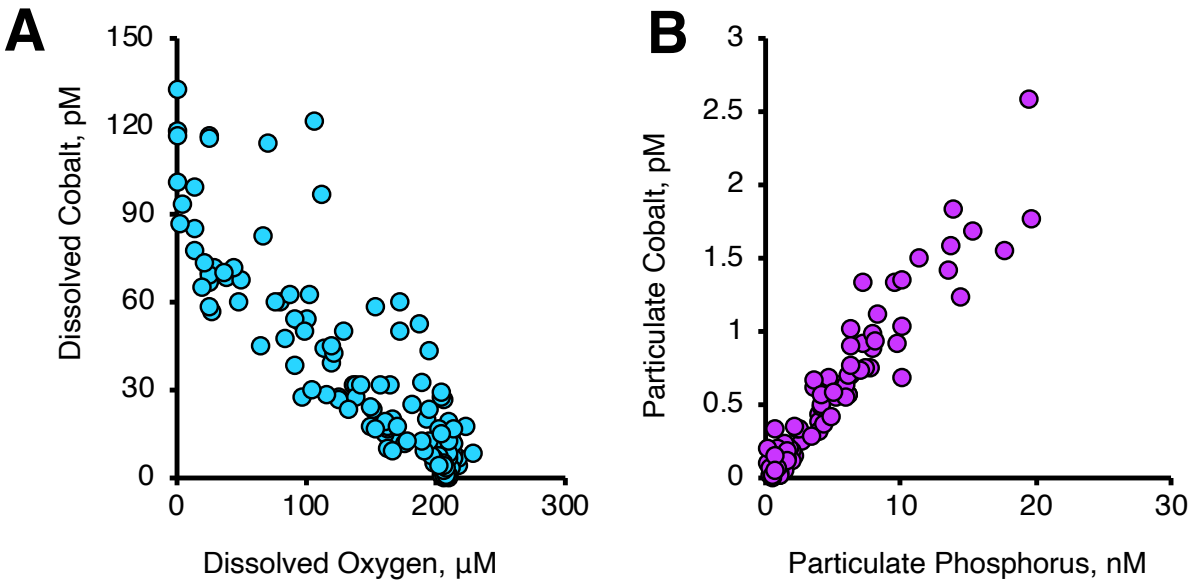

Figure S3. A) Relationship between dissolved cobalt and dissolved oxygen concentration for samples from 0–500 m from the Metzyme cruise (KM1128). B) Relationship between particulate cobalt and particulate phosphorus, also from samples between 0–500 m (note samples with elevated concentrations of both elements are all from the upper 100 m). The slope of this relationship is 110×10^{-6} ($R^2 = 0.92$).

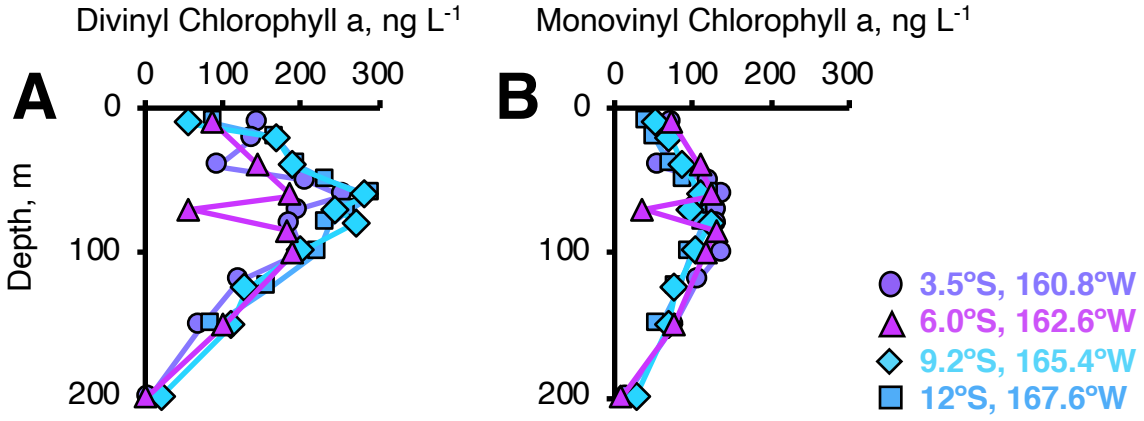

Figure S4. Profiles of divinyl chlorophyll a (A) and monovinyl chlorophyll (B) during the Metzyme cruise, October 2011 (KM1128) for stations in the South Pacific. The divinyl chlorophyll *a* pigment is unique to *Prochlorococcus* and exceeds monovinyl chlorophyll *a* (synthesized by other phytoplankton) for each of these stations. Symbols and color scheme match those in Figure 3A-D. Note that the increase of both chlorophyll types with depth represents an increase in chlorophyll:C ratios (as a response to decreasing light), and not an increase in biomass. Studies in the North Pacific subtropical gyre have emphasized that *Prochlorococcus* growth rates are fastest in the mixed layer (24), where HLII *Prochlorococcus* ecotypes are most abundant (25).

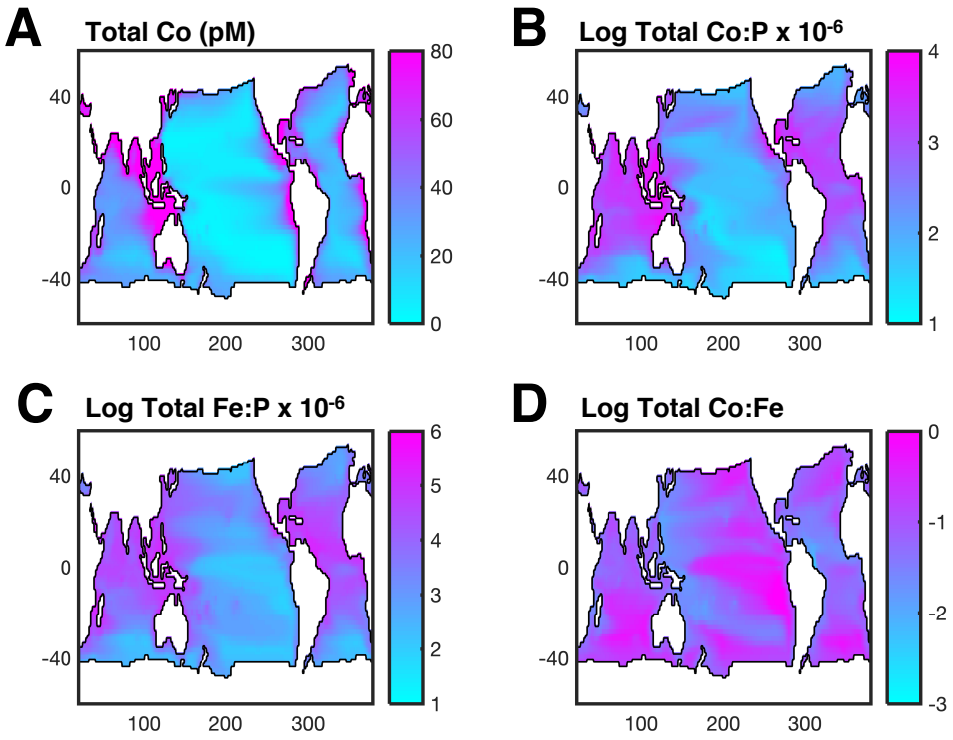

Figure S5. Investigations of surface ocean Co, Fe and P stoichiometry in the PISCES biogeochemical model over the *Prochlorococcus* habitat (defined as waters with temperatures >12C). A) Modelled distribution of total cobalt (sum of dissolved and particulate fields). B) The ratio of total cobalt (panel A) to total phosphorus (the sum of seawater phosphate and particulate fields). C) The ratio of total Fe to total phosphorus. Note that this does not include refractory Fe pools from dust, which are not explicitly modelled here. D) the ratio of total cobalt to total Fe.

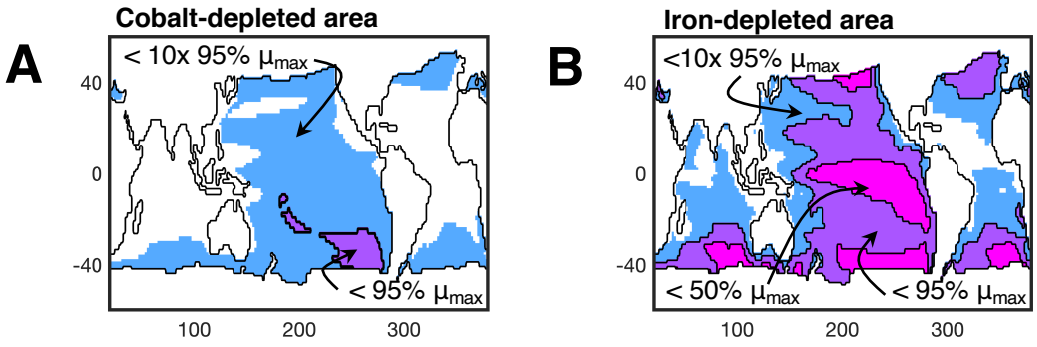

Figure S6. A) Distribution of cobalt poor environments within the PISCES biogeochemical model in the surface ocean. Purple shading indicates surface waters that are depleted in cobalt, having a $Co:PO_4$ ratio below the 95% μ_{max} threshold of *Prochlorococcus* MIT9215 (26×10^{-6}, Table S1). Blue shading indicates regions where $Co:PO_4$ ratios are less than a factor of 10 above the 95% μ_{max} threshold (i.e. $26 < Co:PO_4 < 260 \times 10^{-6}$). The value of 260×10^{-6} corresponds to Co:P ratios in zinc-starved *Emiliana huxleyi* (26). B) Distribution of iron poor environments. Purple and blue regions are defined as in A, representing 95% μ_{max} and 10x 95% μ_{max}. Pink regions highlight areas with a modelled $Fe:PO_4$ ratio below a 50% μ_{max} threshold of *Prochlorococcus* MIT9215.

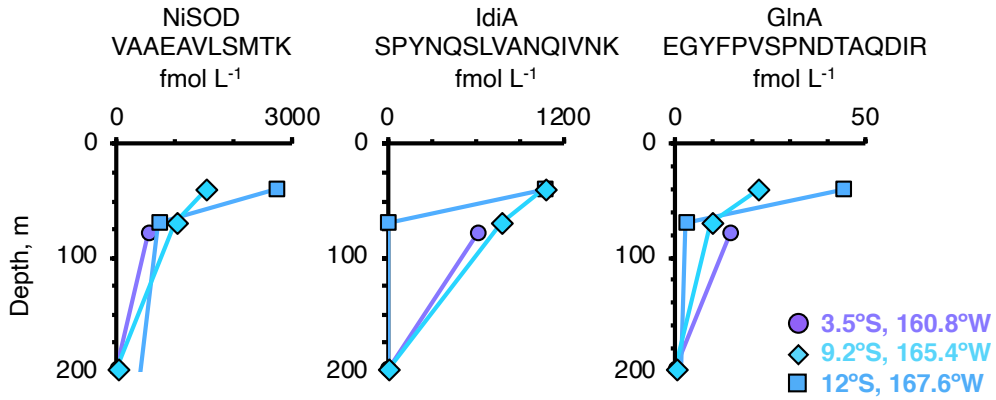

Figure S7. Profiles of *Prochlorococcus*-specific proteins in the South Pacific Gyre from the Metzyme expedition (October 2011). Peptides corresponding to the nickel-dependent superoxide dismutase (NiSOD), the iron deficiency induced protein (IdiA), and Glutamine Synthetase (GlnA) are shown. The abundance of the IdiA protein, which may be an inorganic iron transporter, is indicative of Fe stress (27). These profiles also suggest that *Prochlorococcus* activity is greater near the mixed layer than in the deep chlorophyll maximum layer (75–125 m; Fig. S4). Original data are described by Saito et al. (2014) (15) and can be accessed at https://www.bco-dmo.org/dataset/646115.

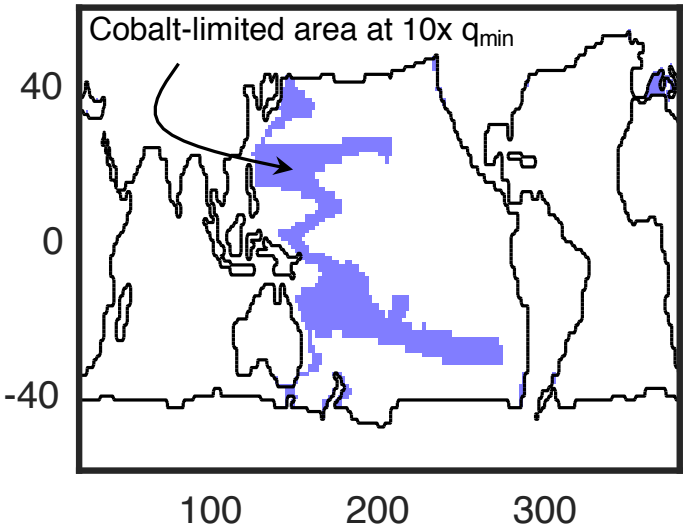

Figure S8. Predicted regions of *Prochlorococcus* cobalt limitation if minimum cobalt requirements were 10-fold higher than measured values, as found in *Emiliana huxleyi* grown in low Zn media. Under these conditions, cobalt limitation is expected to exceed iron and macronutrient limitation for ~12% of surface waters >12°C. The distribution of cobalt depleted waters at this threshold is considerably larger (~55%, Figure S6) but Fe is more strongly depleted in most of that area.

GGATCCATGACACCAGAATTTCTCCGGAGCGTGAGCGAAGTGGGCATTACCCCGAAAACACCAGAATTCCTTCGCGGC
TTTGGCGGCATGGCGAACCCGATTAAAACTCCTGAATTTCTGCGTGTGGCGAGCCTGCTGGGCAAAACACCAGAATT
TCTCCGGGTGTATCATACCAAACCGAGCTATCAGACCATTCTGGATGCGGTGACCAAAACTCCTGAATTCCTTCGCG
AAAACGAAATTGAAGATCTGAGCCGCACACCAGAGTTCCTCCGGTTTAGCGCGAACGCGACCTTTCCGCGCACTCCT
GAATTCCTCCGGTTTGTGGCGGGCAGCATTGGCCCGACCACCAAAACACCAGAGTTTCTGCGTGCGGGCCTGGATAG
CGCGATTATTGCGCCGAACAAAACTCCGGAATTCCTGCGTGCGTTTCAGGATCTGAGCATTCAGGATTTTAAAACCC
CCGAATTCCTTCGCATTAGCCAGTTTAACTTTCCGCGCACTCCCGAATTCCTGCGCGTGAGCGATAGCAACATTCAG
CTGAGCCTGCTGGATGCGAAAACCCCCGAATTTCTCCGGGTGGATCTGAGCACCATGGAAGAAAGCAGCTGGACCGC
GAGCCTGACCAAAACGCCGGAGTTCCTCCGTTTTCTGGAAGTGAACGGCGATTGGATGGCGACCCATCGCACCCCCG
AATTTCTGCGTCATAGCGAATTTAACATTAACCCGCTGTTTCGCACCCTGGAATTTCTGCGCGTGGAAGCGGATATT
GCGGGCCATGGCCAGGAAGTGCTGATTCGCACCCCTGAGTTTCTTCGTCTGTTTACCGGCCATCCGGAAACCCTGGA
AAAAACACCAGAGTTTCTGCGTGGCCATCATGAAGCGGAACTGAAACCGCTGGCGCAGAGCCATGCGACCAAAACTC
CGGAATTCCTGCGTCATCCGGGCGATTTTGGCGCGGATGCGCAGGGCGCGATGACCAAAACTCCTGAATTTCTGCGT
GCGCTGGAACTGTTTCGCACCCCTGAGTTTCTTCGTGAACTGGGCTTTCAGGGCACTCCTGAATTCCTTCGCTTACTC
GAG

Figure S9. Plasmid Sequence used for cloning ^{15}N-labeled peptides for *Prochlorococcus* MIT9215 NrdJ and MetH enzymes. Color scheme: Yellow: Restriction enzymes (5'BamH1, 3'Xho1), Blue: Start/Stop codons, Green: NrdJ peptides, Cyan: MetH peptides, Pink: peptides associated with a *Prochlorococcus* protein of unknown function, Grey: myoglobin, spacer peptides (colorless).

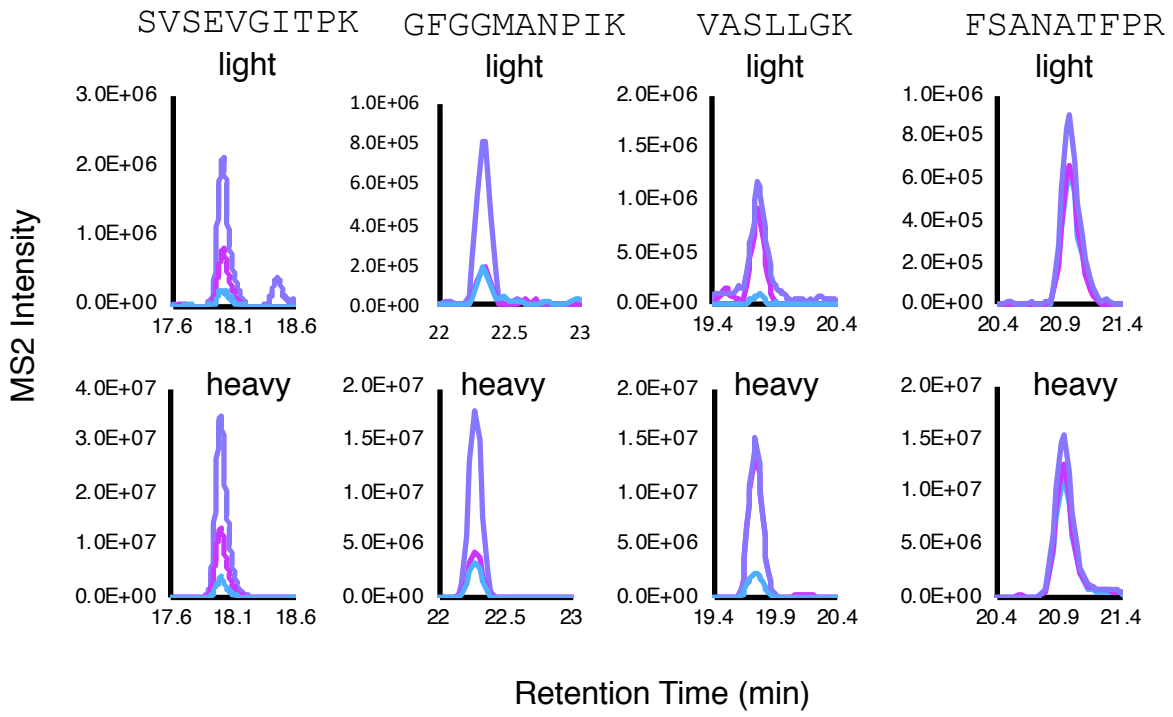

Figure S10. Peptide chromatograms for the ribonucleotide triphosphate reductase from *Prochlorococcus* MIT9215 (NrdJ, 9215_07641). Upper panels show light (unlabeled) peptides deriving from *Prochlorococcus* MIT9215 biomass. Lower panel shows chromatograms for heavy (labeled) peptides. Different lines represent prominent ms^2 fragments. Color coding is consistent between upper and lower panels.

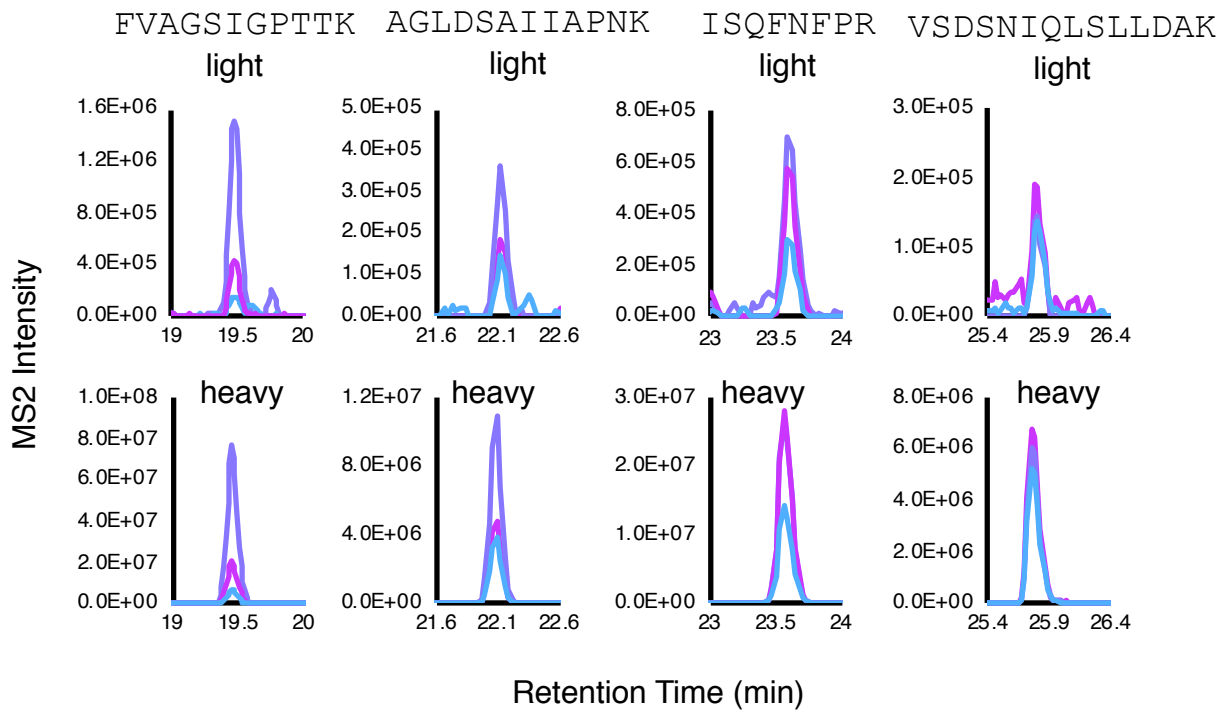

Figure S11. Peptide chromatograms for the methionine synthase from *Prochlorococcus* MIT9215 (MetH, P9215_10151). Upper panels show light (unlabeled) peptides deriving from *Prochlorococcus* MIT9215 biomass. Lower panel shows chromatograms for heavy (labeled) peptides. Different lines represent prominent ms^2 fragments. Color coding is consistent between upper and lower panels.

3. Supplemental Tables

Table S1. Cobalt and iron limitation thresholds of *Prochlorococcus* MIT9215. Values of q_{min} are derived from least-squares regressions to the Droop Equation (Eq. 1 in main text) using the data in Table S2. Separate regressions were derived for cell quota (atom cell^{-1}), metal:P and metal:C ratios (resulting in different R^2). Empirical metal use efficiencies, in mol C day^{-1} (mol metal)$^{-1}$, are calculated as the maximum ratio of growth rate (μ) over the metal:C ratio.

	Co cell^{-1}	Co:P	Co:C	Fe cell^{-1}	Fe:P	Fe:C
q_{min} ($\mu = 0$)	14.8 ± 1.3	1.34 ± 0.09 x 10^{-6}	6.05 ± 0.49 x 10^{-9}	1550 ± 170	0.26 ± 0.04 x 10^{-3}	0.81 ±0.10 x 10^{-6}
20x q_{min} ($\mu = 0.95\ \mu_{max}$)	296 ± 26	26.7 ± 1.83 x 10^{-6}	121± 9.83 x 10^{-9}	31,000 ± 3400	5.17 ± 0.79 x 10^{-3}	16.2 ± 2.05 x 10^{-6}
R^2	0.955	0.972	0.961	0.956	0.916	0.943
Use efficiency (empirical)**			1.55 x 10^7			1.52 x 10^5

*μ_{max} Fe= 0.57; μ_{max} Co = 0.55

** = max(μ/metal:C).

Table S2. Contents of *Prochlorococcus* MIT9215 in unwashed cells under cobalt and iron limitation. Bolded values are used to calculate empirical metal use efficiencies in Table S1. Metal:C ratios are calculated assuming a C quota of 1.85 ± 0.23 x 10^9 C atoms $cell^{-1}$ and a P:C ratio of 325 ± 74 mol:mol (the two approaches are averaged).

[Co] total nM	[Co'] pM	[Fe] total nM	[Fe'] pM	μ day^{-1}	σ	Co atoms $cell^{-1}$	σ	Co:C ratio $x10^{-9}$	σ	Fe atoms $cell^{-1}$	σ	Fe:C ratio $x10^{-6}$	σ	P atoms $cell^{-1}$	σ
10.01	15.50	12	134.7	0.549	0.042	779.9	157.8	321	106	51307	10439	21.1	7.0	1.08E7	2.22E6
3.01	4.66	12	134.7	0.548	0.039	236.4	47.3	103	34	46202	9333	20.1	6.7	9.25E6	1.87E6
1.01	1.56	12	134.7	0.429	0.048	72.2	14.6	39.8	9.9	54760	11129	22.6	7.5	1.07E7	2.17E6
0.61	0.95	12	134.7	**0.329**	**0.021**	**54.0**	**10.8**	**21.2**	**7.0**	**79901**	**15984**	**31.4**	**10.3**	**1.25E7**	**2.51E6**
0.31	0.48	12	134.7	0.086	0.012	16.7	7.0	6.84	4.19	166841	43739	68.2	27.6	1.15E7	4.14E6
0.11	0.17	12	134.7	0.026	0.018										
5.01	7.76	10.3	115.7	0.561	0.018	341.0	68.8	147	48	38258	7657	16.4	5.4	9.61E6	1.92E6
5.01	7.76	3.3	37.1	0.526	0.019	264.6	53.1	132	44	21283	4258	10.6	3.5	6.70E6	1.34E6
5.01	7.76	1.3	14.6	0.477	0.036	240.4	48.1	127	42	12568	2514	6.66	2.19	5.91E6	1.18E6
5.01	7.76	0.6	6.7	**0.402**	**0.025**	**272.8**	**56.0**	**141**	**48**	**5108**	**1140**	**2.64**	**0.91**	**6.21E6**	**1.38E6**
5.01	7.76	0.4	4.5	0.234	0.055										

Table S3. Iron Use efficiency calculations for *Prochlorococcus*

Quantity		**Units**	**Reference, Derivation**
Iron atoms in Photosynthetic chain	20 (23*)	Atoms per photosynthetic complex	Raven 1990 (28)
Turnover time of PSII	250	Electrons per s	Raven 1988 (29)
Electrons per CO2 fixed	4	Electrons	C(+4)O2 → C(0)H2O
Ratio CO2 fixed per C biomass	1.333	Mol : mol	Raven 1988 (29)
Iron Use efficiency, photosynthesis (24 hour light)	0.427 (0.491*)	Mol Fe per (mol C per s)	= 1.333 x 4 x 20 / 250
Iron Use efficiency, photosynthesis (14:10)	0.731 (0.841*)	Mol Fe per (mol C per s)	= 0.427 x 24 / 14
Iron atoms in respiration	42	Atoms per respiratory complex	Raven 1988 (29)
Turnover time respiratory cytochrome C oxidase	250	Electrons per s	Raven 1988 (29)
Iron Use efficiency, respiration	0.224	Mol Fe per (mol C per s)	= (1.333–1) x 4 x 42 / 250
Total Iron use efficiency	0.955 (1.065*)	Mol Fe per (mol C per s)	= 0.731 + 0.224
	9.04×10^4 (8.11×10^4*)	Mol C per day per mol Fe	= 86400 / 0.955
C per cell	1.85×10^9		Martiny et al. 2016 (8)
Growth Rate (arbitrary)	0.4	Per day	
Fe quota, predicted	8200 (9140*)	Fe Atoms Per cell	= $0.4 \times 1.85 \times 10^9 / 9.04 \times 10^4$
Fe quota, measured	5108 ± 1140	Fe Atoms Per cell	Table S2

*including Fe use in Ferredoxin and Cytochrome C (versus substitution by Flavodoxin and Plastocyanin); assumes equimolar photosynthetic stoichiometry (i.e. PSI:PSII = 1)

Table S4. Cobalt Use Efficiency calculations for *Prochlorococcus*

Quantity		Units	Reference or derivation
Co:NrdJ stoichiometry	1	Mol Co : mol NrdJ	Sintchak et al. 2002 (30)
NrdJ Turnover time	2	Bases Per second	Licht et al. 1999 (13)
NrdJ output, daily	1.73×10^5	Bases per day per NrdJ	= 2 x 60 x 60 x 24
Genome size	3.4×10^6	dNTP bases*	Kettler et al. 2007 (31)
NrdJ demand	20.1	Copies NrdJ per cell per day	$= 3.4 \times 10^6 / 1.7 \times 10^5$
Co demand, nrdJ	20.1	Co per cell per day	
Co:MetH stoichiometry	1	Mol Co:mol MetH	Drennan et al. 1994 (32)
MetH turnover time	18	Methionine molecules per second	Banerjee et al. 1990 (33)
MetH output, daily	1.6×10^6	Methionine molecules per day	= 18 x 60 x 60 x 24
Maximum methionine molecules per cell	1.2×10^7	Sulfur atoms per cell	Assuming P:S ratio ~ 1 Heldal et al. 2003 (34)
Methionine demand	7.7	Copies met H per cell per day	$= 1.2 \times 10^7 / 1.6 \times 10^6$
Co demand, metH	7.7	Co per cell per day	
C per cell	1.85×10^9	Atoms per cell	Martiny et al. 2016 (8)
Co Use efficiency, calculated	6.6×10^7	Mol C per day per mol Co	$= 1.85 \times 10^9 / (20.1 + 7.7)$
Co Use efficiency, empirical	1.55×10^7	Mol C per day per mol Co	Table S1
Growth Rate (μ_{max})	0.20 (0.6)	Per day	Table S2
NrdJ quota, predicted	4.0 (11.8)	Copies per cell	= 0.2 x 20.1
NrdJ quota, measured	15 ± 2	Copies per cell	
MetH quota predicted	1.5 (4.8)	Copies per cell	= 0.2 x 7.7
MetH quota measured	7 ± 2	Copies per cell	
Co quota, predicted	5.5 (16.6)	Atoms per cell	= 4 + 1.5
Co quota, measured	65 ± 8	Atoms per cell	

*1.7 million base pairs

Table S5. Peptide and DNA sequences of used in plasmid construction.

Ribonucleotide reductase NrdJ	
SVSEVGITPK	AGCGTGAGCGAAGTGGGCATTACCCCGAAA
GFGGMANPIK	GGCTTTGGCGGCATGGCGAACCCGATTAAA
VASLLGK	GTGGCGAGCCTGCTGGGCAAA
VYHTKPSYQTILDAVTK	GTGTATCATACCAAACCGAGCTATCAGACCATTCTGGATGCGGTGACCAAA
SLLTGAAPGWHPPK	AGCCTGCTGACCGGCGCGGCGCCGGGCTGGCATCCGCCGAAA
ENEIEDLSR	GAAAACGAAATTGAAGATCTGAGCCGC
FSANATFPR	TTTAGCGCGAACGCGACCTTTCCGCGC
YDVGELSEAGPAGCDSDK	TATGATGTGGGCGAACTGAGCGAAGCGGGCCCGGCGGGCTGCGATAGCGATAAA

Methionine synthase MetH	
ELEGCNENLVLSSPNVVER	GAACTGGAAGGCTGCAACGAAAACCTGGTGCTGAGCAGCCCGAACGTGGTGGAACGC
FVAGSIGPTTK	TTTGTGGCGGGCAGCATTGGCCCGACCACCAAA
AGLDSAIIAPNK	GCGGGCCTGGATAGCGCGATTATTGCGCCGAACAAA
AFQDLSIQDFK	GCGTTTCAGGATCTGAGCATTCAGGATTTTAAA
INLNSIFLDECIK	ATTAACCTGAACAGCATTTTTCTGGATGAATGCATTAAA
ISQFNFPR	ATTAGCCAGTTTAACTTTCCGCGC
YSFGYPACPK	TATAGCTTTGGCTATCCGGCGTGCCCGAAA
VSDSNIQLSLLDAK	GTGAGCGATAGCAACATTCAGCTGAGCCTGCTGGATGCGAAA

Myoglobin	
VEADIAGHGQEVLIR	GTGGAAGCGGATATTGCGGGCCATGGCCAGGAAGTGCTGATTCGC
LFTGHPETLEK	CTGTTTACCGGCCATCCGGAAACCCTGGAAAAA
GHHEAELKPLAQSHATK	GGCCATCATGAAGCGGAACTGAAACCGCTGGCGCAGAGCCATGCGACCAAA
HPGDFGADAQGAMTK	CATCCGGGCGATTTTGGCGCGGATGCGCAGGGCGCGATGACCAAA
ALELFR	GCGCTGGAACTGTTTCGC
ELGFQG	GAACTGGGCTTTCAGGGC

Table S6. Calibration of ^{15}N labeled myoglobin peptides to 100 fmol ^{14}N myoglobin peptides. Duplicate injections shown.

Peptide Sequence	Injection Number	Peptide Peak Found Ratio	Peptide Retention Time (minutes)	Ratio To Standard
VEADIAGHGQEVLIR	1	1	21.83	2.4049
VEADIAGHGQEVLIR	2	1	21.68	2.3136
LFTGHPETLEK	1	1	19.71	2.6456
LFTGHPETLEK	2	1	19.47	2.7566
GHHEAELKPLAQSHATK	1	1	15.33	2.5027
GHHEAELKPLAQSHATK	2	1	14.87	2.1853
ALELFR	1	1	25.98	2.7962
ALELFR	2	0.94	25.92	2.9433
HPGDFGADAQGAMTK	1	1	18.9	4.1635
HPGDFGADAQGAMTK	2	1	18.6	4.1598
Median				2.701

Table S7. Quantitation of MetH and NrdJ peptides in large volume *Prochlorococcus* cultures and comparison to cobalt quotas measured by ICP-MS. Measurements of strongly limited cells (μ = 0.2 day^{-1}) are shown in Figure 1C.

Growth Rate (day^{-1})	Abundance (cells ml^{-1})	Cobalt (atoms cell^{-1})	Ribonucleotide reductase NrdJ (copies per cell ± 1SD)									
			SVSEVGITPK		GFGGMANPIK		VASLLGK		FSANATFPR		**Mean**	**±**
0.2	5.7E+07	98	13.5	0.1	12.6	0.2	15.4	0.1	14.3	0.2	13.9	1.2
0.2	6.9E+07	86	15.6	0.3	12.5	0.2	17.8	1.0	14.3	0.3	15.0	2.2
0.2	1.0E+08	72	11.6	0.0	13.5	0.2	15.2	1.7	12.3	0.1	13.2	1.6
0.32	4.6E+07	70	11.3	0.1	8.7	0.4	12.0	0.1	11.3	0.3	10.8	1.5
0.32	9.7E+07	65	10.8	0.3	9.4	0.1	12.6	0.4	10.4	0.4	10.8	1.4
0.32	1.3E+08	62	15.1	0.2	12.5	0.4	16.2	0.6	14.5	0.6	14.6	1.6

			Methionine Synthase MetH (copies per cell ± 1SD)									
			FVAGSIGPTTK		AGLDSAIIAPNK		ISQFNFPR		VSDSNIQLSLLDAK		**Mean**	**±**
0.2	5.7E+07	98	4.2	0.2	7.8	0.1	5.0	0.0	5.4	0.1	5.6	1.6
0.2	6.9E+07	86	5.7	0.4	9.5	0.3	6.7	0.7	7.3	0.8	7.3	1.6
0.2	1.0E+08	72	4.3	0.4	6.9	0.1	4.7	0.5	5.6	0.2	5.4	1.1
0.32	4.6E+07	70	5.6	0.1	8.9	0.1	6.1	0.0	7.4	0.4	7.0	1.5
0.32	9.7E+07	65	5.2	0.2	9.1	1.0	5.7	0.3	7.0	0.6	6.8	1.8
0.32	1.3E+08	62	8.2	0.5	14.8	0.3	9.1	0.2	12.4	0.4	11.2	3.0

Table S8. Spectral counting of *Prochlorococcus* MIT9215 proteomes from the cobalt gradient experiment. Only proteins identified in all cobalt-limited (0.6 and 1 nM) or in all cobalt-replete (10 and 3 nM) samples are shown. Fisher exact tests compare Cobalt Replete and Cobalt Limited groups.

Identified proteins n = 484								
Significant proteins n = 56 (Fischer exact p<0.01)	Cobalt Replete				Cobalt Limited			
	10 nM		3 nM		1 nM		600 pM	
Upregulated proteins (n=20, Fisher exact p<0.01)	A	B	A	B	A	B	A	B
50S ribosomal protein L20	3	8	6	2	**15**	**33**	**4**	**13**
Photosystem II manganese-stabilizing protein	20	48	34	39	**60**	**88**	**73**	**62**
60 kDa chaperonin 2	113	142	73	66	**172**	**157**	**134**	**148**
50S ribosomal protein L2	71	111	85	80	**176**	**169**	**119**	**136**
Helix-hairpin-helix DNA-binding protein containing motif class 1	5	2	4	0	**21**	**16**	**11**	**3**
Thioredoxin	36	60	38	46	**69**	**85**	**79**	**77**
50S ribosomal protein L7/L12	25	28	34	29	**56**	**50**	**58**	**51**
ATP synthase subunit b	7	13	16	13	**19**	**35**	**29**	**26**
Photosystem I protein PsaD	37	40	24	21	**81**	**70**	**44**	**24**
Putative Branched-chain amino acid aminotransferase	24	20	12	14	**37**	**39**	**33**	**31**
Ribulose bisphosphate carboxylase, small chain	150	120	99	129	**113**	**161**	**95**	**131**
50S ribosomal protein L16	17	12	6	10	**29**	**32**	**18**	**17**
Ferritin	15	12	13	9	**32**	**17**	**35**	**18**
Histone-like DNA-binding protein	62	137	74	130	**121**	**178**	**143**	**153**
50S ribosomal protein L19	45	67	41	24	**88**	**74**	**75**	**47**
50S ribosomal protein L15	23	16	15	23	**32**	**37**	**28**	**42**
Single-stranded DNA-binding protein	7	11	0	14	**12**	**22**	**13**	**23**
Nucleoside diphosphate kinase	18	12	10	0	**25**	**18**	**24**	**14**
Putative DNA-directed RNA polymerase (omega chain)	19	47	24	35	**49**	**62**	**46**	**47**
Protein GrpE	30	41	46	21	**66**	**59**	**62**	**32**
Downregulated proteins (n=14, Fisher exact p<0.01)								
D-fructose 1,6-bisphosphatase class 2/sedoheptulose 1,7-bisphosphatase	**42**	**110**	**24**	**14**	65	33	40	16
Uncharacterized protein	**75**	**52**	**77**	**64**	63	48	63	55
Ribulose bisphosphate carboxylase large chain	**22**	**44**	**16**	**16**	28	12	2	8
Transketolase	**75**	**59**	**45**	**44**	30	45	6	3
30S ribosomal protein S16	**23**	**48**	**28**	**46**	32	51	12	7
30S ribosomal protein S4	**13**	**25**	**18**	**12**	13	6	4	0
ATP synthase gamma chain	**17**	**19**	**10**	**11**	15	7	3	0
Putative nicotinamide nucleotide transhydrogenase, subunit alpha 1 (A1)	**9**	**7**	**3**	**4**	3	2	0	0
ATP synthase subunit beta	**100**	**121**	**78**	**89**	104	124	64	70
30S ribosomal protein S13	**24**	**14**	**10**	**8**	10	9	8	6
30S ribosomal protein S3	**6**	**5**	**5**	**2**	5	0	0	0
50S ribosomal protein L11	**10**	**21**	**6**	**11**	11	5	10	3
30S ribosomal protein S10	**13**	**11**	**5**	**13**	9	15	2	0
Thioredoxin peroxidase	**16**	**14**	**0**	**5**	7	5	3	6
Not significantly regulated proteins (n=87, p>0.01)								
Ferredoxin-NADP oxidoreductase (FNR)	36	39	19	25	31	41	28	8
50S ribosomal protein L17	25	29	24	21	51	43	37	27

	10 nM		3 nM		1 nM		600 pM	
Not significantly regulated proteins (continued)	A	B	A	B	A	B	A	B
ABC-type Fe3+ transport system, periplasmic component	21	25	12	16	42	35	22	24
50S ribosomal protein L18	15	53	36	31	49	73	40	45
50S ribosomal protein L35	9	7	8	13	15	17	15	22
Uncharacterized protein	8	8	10	7	11	21	24	7
50S ribosomal protein L27	8	7	8	5	8	6	4	0
Protoporphyrin IX Magnesium chelatase, ChlI subunit	22	10	4	3	16	6	7	0
10 kDa chaperonin	9	13	7	6	19	19	19	7
ATP synthase subunit alpha	65	67	36	42	67	73	36	39
Possible cAMP phosphodiesterase class-II	6	6	0	0	9	9	7	3
50S ribosomal protein L23	8	13	9	3	21	17	10	12
30S ribosomal protein S7	29	39	33	33	53	49	18	11
Elongation factor Tu	99	133	52	100	74	91	111	137
Triosephosphate isomerase	21	29	20	2	31	30	0	4
Uncharacterized protein	18	19	23	24	26	41	39	23
NifU-like protein	4	8	7	2	7	8	14	10
Signal peptide peptidase SppA (Protease IV)	10	3	2	4	16	8	9	4
Photosystem I iron-sulfur center	17	19	20	23	46	23	24	28
Chaperone protein DnaK	34	37	26	9	41	26	27	11
Ribosomal protein S1	24	28	17	11	26	23	18	10
Carboxysome shell protein CsoS2	37	41	49	29	73	47	62	39
Putative nickel-containing superoxide dismutase (NISOD)	10	14	6	8	9	6	11	7
Glutamate-1-semialdehyde 2,1-aminomutase	10	12	5	5	11	7	4	5
Pyridoxine 5'-phosphate synthase	9	6	11	9	15	10	15	17
50S ribosomal protein L13	18	18	11	7	24	23	15	20
Ornithine carbamoyltransferase, catabolic	8	10	15	2	14	18	15	9
Dihydrolipoyl dehydrogenase	17	11	8	3	15	13	6	2
Enolase	25	22	10	6	39	20	16	18
Uncharacterized protein	2	5	6	3	6	4	0	2
Elongation factor P	12	11	15	4	16	10	12	2
Glutamine synthetase	58	142	56	76	114	101	126	94
Flavodoxin	6	16	4	15	11	20	16	15
Delta-aminolevulinic acid dehydratase	8	7	0	5	8	14	2	8
Photosystem I PsaF protein (Subunit III)	20	12	7	3	25	16	0	0
50S ribosomal protein L1	12	9	8	11	15	9	10	5
50S ribosomal protein L24	9	0	2	0	7	7	4	2
Uncharacterized protein	29	13	6	5	24	14	10	6
Uncharacterized protein	14	11	7	12	19	18	14	13
Carboxysome shell protein CsoS1	243	329	142	243	326	307	249	245
Uncharacterized protein	14	15	6	6	20	16	16	8
Polyribonucleotide nucleotidyltransferase	20	13	8	9	14	15	11	11
Fructose-bisphosphate aldolase	20	31	20	15	50	29	7	6
50S ribosomal protein L4	72	212	107	97	193	153	129	92
Uncharacterized protein	20	36	25	20	32	24	31	24
DNA-directed RNA polymerase subunit beta'	24	14	5	0	18	15	6	5
S-adenosylmethionine synthase	15	23	13	10	25	23	10	7
50S ribosomal protein L32	9	7	8	9	7	4	14	8
50S ribosomal protein L14	21	14	15	11	25	13	20	7
Cell division protein FtsZ	32	49	24	18	52	41	38	32
50S ribosomal protein L3	20	22	8	7	26	26	16	11
30S ribosomal protein S5	17	12	6	10	20	24	3	0
Soluble hydrogenase small subunit	9	5	0	5	6	8	7	8
50S ribosomal protein L9	15	19	8	18	21	24	17	20
50S ribosomal protein L29	4	11	2	3	8	9	8	5
50S ribosomal protein L6	33	26	27	21	42	30	22	26

	10 nM		3 nM		1 nM		600 pM	
Not significantly regulated proteins (continued)	A	B	A	B	A	B	A	B
Ribosome-recycling factor	7	0	3	4	9	2	6	5
60 kDa chaperonin 1	31	18	8	8	32	19	9	11
Putative IMP dehydrogenase	49	60	42	70	71	92	51	41
30S ribosomal protein S15	10	15	9	3	19	28	5	0
30S ribosomal protein S6	17	17	28	9	36	19	23	0
Two-component response regulator	20	14	11	11	24	17	21	14
3-oxoacyl-[acyl-carrier-protein] synthase 2	9	8	6	6	12	8	6	4
Two-component response regulator	8	7	2	3	10	5	3	2
ATP-dependent zinc metalloprotease FtsH	7	11	6	3	15	12	5	6
50S ribosomal protein L28	9	6	4	3	15	11	2	3
Photosystem II lipoprotein Psb27	11	5	7	4	12	7	8	2
ATP synthase subunit b'	14	8	8	3	15	5	9	7
Light-harvesting complex protein	12	10	4	6	11	13	11	8
Putative GTP cyclohydrolase I	11	9	7	9	15	14	8	11
Photosystem II D2 protein	5	5	4	4	6	13	0	0
Phosphate-binding protein	11	16	16	11	23	15	18	14
30S ribosomal protein S14	22	42	14	12	37	29	23	16
30S ribosomal protein S18	8	7	9	13	16	15	13	5
ATP-dependent zinc metalloprotease FtsH	14	8	7	7	15	15	7	10
Actin-like ATPase involved in cell morphogenesis	15	21	10	16	11	20	18	30
Photosystem II reaction center Psb28 protein	15	29	17	40	29	35	32	30
Biotin carboxyl carrier protein	9	16	6	11	11	20	9	9
Glyceraldehyde-3-phosphate dehydrogenase	14	10	3	4	17	9	7	7
Uncharacterized protein	11	8	9	6	11	14	7	8
50S ribosomal protein L5	17	19	17	14	23	25	13	19
Peptidyl-prolyl cis-trans isomerase	36	41	26	25	38	54	35	31
Putative potassium channel, VIC family	6	7	4	0	6	3	9	4
DNA-directed RNA polymerase subunit alpha	66	62	33	53	85	61	70	46
Pentapeptide repeat-containing proteins	20	24	6	11	16	33	16	10
Cysteine synthase	5	9	2	0	5	5	4	5
DNA-directed RNA polymerase subunit beta	12	9	6	0	11	8	8	6